

DESI EDR: Calibrating the Tully-Fisher Relationship with the DESI Peculiar Velocity Survey

K. DOUGLASS,¹ S. BENZVI,¹ N. UBEROI,² C. HOWLETT,³ C. SAULDER,⁴ K. SAID,³ R. DEMINA,¹ J. AGUILAR,⁵ S. AHLEN,⁶
G. ALDERING,⁵ D. BIANCHI,^{7,8} D. BROOKS,⁹ T. CLAYBAUGH,⁵ A. CUCEU,⁵ T. M. DAVIS,³ K. S. DAWSON,¹⁰
A. DE LA MACORRA,¹¹ A. FONT-RIBERA,¹² J. E. FORERO-ROMERO,^{13,14} E. GAZTAÑAGA,^{15,16,17}
S. GONTCHO A GONTCHO,^{5,18} G. GUTIERREZ,¹⁹ C. HAHN,²⁰ K. HONSCHIED,^{21,22} M. ISHAK,²³ R. JOYCE,²⁴ T. KISNER,⁵
A. KREMIN,⁵ M. LANDRIAU,⁵ M. E. LEVI,⁵ J. LUCEY,²⁵ P. MARTINI,^{21,26} A. MEISNER,²⁴ R. MIQUEL,^{27,12} J. MOUSTAKAS,²⁸
N. PALANQUE-DELABROUILLE,^{29,5} W. J. PERCIVAL,^{30,31,32} F. PRADA,³³ G. ROSSI,³⁴ E. SANCHEZ,³⁵ D. SCHLEGEL,⁵
M. SCHUBNELL,³⁶ J. SILBER,⁵ D. SPRAYBERRY,²⁴ G. TARLÉ,³⁶ B. A. WEAVER,²⁴ R. ZHOU,⁵ AND H. ZOU³⁷

¹*Department of Physics & Astronomy, University of Rochester, 500 Joseph C. Wilson Blvd., Rochester, NY 14627, USA*

²*Physics Department, Yale University, P.O. Box 208120, New Haven, CT 06511, USA*

³*School of Mathematics and Physics, University of Queensland, Brisbane, QLD 4072, Australia*

⁴*Max Planck Institute for Extraterrestrial Physics, Gießenbachstraße 1, 85748 Garching, Germany*

⁵*Lawrence Berkeley National Laboratory, 1 Cyclotron Road, Berkeley, CA 94720, USA*

⁶*Department of Physics, Boston University, 590 Commonwealth Avenue, Boston, MA 02215 USA*

⁷*Dipartimento di Fisica “Aldo Pontremoli”, Università degli Studi di Milano, Via Celoria 16, I-20133 Milano, Italy*

⁸*INAF-Osservatorio Astronomico di Brera, Via Brera 28, 20122 Milano, Italy*

⁹*Department of Physics & Astronomy, University College London, Gower Street, London, WC1E 6BT, UK*

¹⁰*Department of Physics and Astronomy, The University of Utah, 115 South 1400 East, Salt Lake City, UT 84112, USA*

¹¹*Instituto de Física, Universidad Nacional Autónoma de México, Circuito de la Investigación Científica, Ciudad Universitaria, Cd. de México C. P. 04510, México*

¹²*Institut de Física d’Altes Energies (IFAE), The Barcelona Institute of Science and Technology, Edifici Cn, Campus UAB, 08193, Bellaterra (Barcelona), Spain*

¹³*Departamento de Física, Universidad de los Andes, Cra. 1 No. 18A-10, Edificio Ip, CP 111711, Bogotá, Colombia*

¹⁴*Observatorio Astronómico, Universidad de los Andes, Cra. 1 No. 18A-10, Edificio H, CP 111711 Bogotá, Colombia*

¹⁵*Institut d’Estudis Espacials de Catalunya (IEEC), c/ Esteve Terradas 1, Edifici RDIT, Campus PMT-UPC, 08860 Castelldefels, Spain*

¹⁶*Institute of Cosmology and Gravitation, University of Portsmouth, Dennis Sciama Building, Portsmouth, PO1 3FX, UK*

¹⁷*Institute of Space Sciences, ICE-CSIC, Campus UAB, Carrer de Can Magrans s/n, 08913 Bellaterra, Barcelona, Spain*

¹⁸*Department of Astronomy, University of Virginia, Charlottesville, VA 22904, USA*

¹⁹*Fermi National Accelerator Laboratory, PO Box 500, Batavia, IL 60510, USA*

²⁰*Steward Observatory, University of Arizona, 933 N. Cherry Avenue, Tucson, AZ 85721, USA*

²¹*Center for Cosmology and AstroParticle Physics, The Ohio State University, 191 West Woodruff Avenue, Columbus, OH 43210, USA*

²²*Department of Physics, The Ohio State University, 191 West Woodruff Avenue, Columbus, OH 43210, USA*

²³*Department of Physics, The University of Texas at Dallas, 800 W. Campbell Rd., Richardson, TX 75080, USA*

²⁴*NSF NOIRLab, 950 N. Cherry Ave., Tucson, AZ 85719, USA*

²⁵*Institute for Computational Cosmology, Department of Physics, Durham University, South Road, Durham DH1 3LE, UK*

²⁶*Department of Astronomy, The Ohio State University, 4055 McPherson Laboratory, 140 W 18th Avenue, Columbus, OH 43210, USA*

²⁷*Institució Catalana de Recerca i Estudis Avançats, Passeig de Lluís Companys, 23, 08010 Barcelona, Spain*

²⁸*Department of Physics and Astronomy, Siena College, 515 Loudon Road, Loudonville, NY 12211, USA*

²⁹*IRFU, CEA, Université Paris-Saclay, F-91191 Gif-sur-Yvette, France*

³⁰*Department of Physics and Astronomy, University of Waterloo, 200 University Ave W, Waterloo, ON N2L 3G1, Canada*

³¹*Perimeter Institute for Theoretical Physics, 31 Caroline St. North, Waterloo, ON N2L 2Y5, Canada*

³²*Waterloo Centre for Astrophysics, University of Waterloo, 200 University Ave W, Waterloo, ON N2L 3G1, Canada*

³³*Instituto de Astrofísica de Andalucía (CSIC), Glorieta de la Astronomía, s/n, E-18008 Granada, Spain*

³⁴*Department of Physics and Astronomy, Sejong University, 209 Neungdong-ro, Gwangjin-gu, Seoul 05006, Republic of Korea*

³⁵*CIEMAT, Avenida Complutense 40, E-28040 Madrid, Spain*

³⁶*Department of Physics, University of Michigan, 450 Church Street, Ann Arbor, MI 48109, USA*

³⁷*National Astronomical Observatories, Chinese Academy of Sciences, A20 Datun Road, Chaoyang District, Beijing, 100101, P. R. China*

ABSTRACT

We calibrate the Tully-Fisher relation (TFR) with data from the DESI Peculiar Velocity (PV) Survey taken during the Survey Validation (SV) period of the DESI galaxy redshift survey. Placing spectroscopic fibers on the centers and major axes of spatially-extended spiral galaxies identified in the 2020 Siena Galaxy Atlas using the DESI Legacy Surveys, we measure the rotational velocities at $0.33R_{26}$ for 1163 (1136 + 27 dwarf) spiral galaxies observed during SV. Using 41 spiral galaxies observed in the Coma Cluster, we find a slope for the TFR of -7.96 ± 0.13 AB mag in the r -band, with a scatter about the TFR of 1.07 ± 0.02 AB mag. We calibrate the zero-point of the TFR using galaxies with independent distances measured using type Ia supernovae via the cosmological distance ladder. From the SN Ia distances, we measure a zero-point of $-19.34^{+0.30}_{-0.29}$ AB mag in the r -band. We produce a public catalog of the distances to these 1136 spiral galaxies observed during DESI SV as part of the DESI PV Survey with our calibrated TFR. This is, to our knowledge, the first catalog of TFR distances produced with velocities measured at a single point in the disk.

1. INTRODUCTION

Direct measurements of individual galaxy peculiar velocities (PVs) at low redshift have seen a resurgence in recent years, particularly with the advent of large spectroscopic survey programs that can collectively observe millions of galaxies with high signal-to-noise (York et al. 2000; Colless et al. 2001; Jones et al. 2004; Abazajian et al. 2009). PVs have long been used as a way to constrain the growth of structure (Kaiser 1988; Gorski et al. 1989; Groth et al. 1989; Nusser & Davis 1994; Davis et al. 1996; Park 2000; Park & Park 2006; Davis et al. 2011; Johnson et al. 2014; Howlett et al. 2017c; Qin et al. 2019; Howlett 2019; Said et al. 2020; Boruah et al. 2020a; Qin et al. 2021; Turner et al. 2021; Qin et al. 2023; Lai et al. 2023; Turner et al. 2023; Shi et al. 2024). The power of PVs lies in their ability to provide a direct tracer of the matter field without the complications of galaxy bias, and to overcome the so-called ‘‘cosmic variance limit’’ that arises at low redshift when only galaxy redshifts are available (Burkey & Taylor 2004; Koda et al. 2014). Recent studies have demonstrated that combined PV and redshift surveys will likely provide the tightest constraints on the growth of cosmic structure under the influence of gravity in the coming years (Koda et al. 2014; Howlett et al. 2017b; Whitford et al. 2022).

Galaxy PVs can be obtained in a number of ways, but in all cases rely on an empirically-calibrated redshift-independent distance indicator. Well-known examples include Surface Brightness Fluctuations (Tonry & Schneider 1988), Type Ia Supernovae (Phillips 1993), the Fundamental Plane relation (FP; Djorgovski & Davis 1987; Dressler et al. 1987), and the Tully-Fisher relation (TFR; Tully & Fisher 1977). Given a distance indicator, PVs can be extracted from the relative difference between the observed redshift and the cosmological (or recessional) redshift inferred from the distance indicator (Watkins & Feldman 2015; Davis & Scrimgeour 2014). The largest single samples of these various dis-

tance indicators now number from hundreds to several tens of thousands (Boruah et al. 2020b; Kourkchi et al. 2020a,b; Howlett et al. 2022). Combined, the largest currently available catalog is the Cosmicflows-4 compilation of $\sim 55,000$ measurements (Tully et al. 2023b). These data have been used to uncover new structures in our nearby Universe (Graziani et al. 2019; Tully et al. 2023a), and provide new constraints on gravity and the validity of General Relativity (Lai et al. 2023). However, upcoming surveys aim to increase this catalog by a further order of magnitude in both cosmic volume and number of galaxies over the next 5 years (Howlett et al. 2017a; Koribalski et al. 2020; Taylor et al. 2023), promising further discoveries and tighter constraints.

One such example is the Dark Energy Spectroscopic Instrument Peculiar Velocity survey (Saulder et al. 2023). Well into its 5-year program, this survey aims to measure, with the same instrument, PVs using both the FP and TFR methods. Simulations of the efficiency and success rate with which DESI can observe these objects predict that the full survey will contain over 130,000 and 50,000 FP- and TFR-based PVs, respectively, over 14,000 sq. deg. (mostly in the northern hemisphere). Here, we expand on the proof-of-concept provided by Saulder et al. (2023) by producing the first suite of DESI PV measurements using the now publicly available Early Data Release of DESI (DESI Collaboration et al. 2024a). We present the first catalog of 1136 TFR-based PV measurements from DESI, which are scattered across the full footprint but represent only a small fraction of the data to come. Of particular interest, and highlighted further in this work, are deep measurements obtained in and around the Coma Cluster. We demonstrate that the DESI TFR measurements are robust, comparable to those obtained using H I observations and other measurements (Springob et al. 2007; Hong et al. 2019; Kourkchi et al. 2020b). The catalog is already a substantial contribution to the ensemble of available PV measurements, despite accounting for

a small percentage of the data we expect with DESI’s upcoming data releases.

The layout of this paper is as follows. We first introduce the Tully-Fisher relation and its underlying assumptions in Section 2. We then describe the DESI instrument, the DESI Peculiar Velocity Survey, and the DESI Early Data Release (EDR) in Section 3. A description of our Tully-Fisher measurements, our quality selection criteria, and our estimated systematic uncertainties follow in Section 4. Section 5 discusses the calibration of the slope and zero point of the Tully-Fisher relation using data from DESI EDR. The measured Tully-Fisher relation for 1136 galaxies in the DESI EDR is presented in Section 6, followed by a comparison of our calibrated TFR with previous work in Section 7. We conclude in Section 8.

2. THE TULLY-FISHER RELATION

Galaxy redshift surveys, by themselves, are unable to disentangle the two components of the observed galaxy redshift, z_{obs} : the cosmological part due to the smooth expansion of the universe, z_{cosmo} , and the peculiar velocity due to the gravitational attraction of the growing overdensities, z_{pec} (Davis & Scrimgeour 2014):

$$1 + z_{\text{obs}} = (1 + z_{\text{cosmo}})(1 + z_{\text{pec}}) \quad (1)$$

To distinguish between these two components, redshift-independent measurements of the distances are required. This is possible with the use of a distance indicator, a correlation between distance-independent and distance-dependent intrinsic properties of a galaxy.

Due to its simplicity, one of the most successful distance indicators is the Tully-Fisher relation (TFR; Tully & Fisher 1977). The TFR is a correlation between the rotational velocity (distance-independent property) and brightness (distance-dependent property) of a galaxy. Consequently, the TFR is applicable to spiral galaxies, rotationally-supported systems that have an intrinsic relationship between their rotational velocity and luminosity.

While there is no unanimity on the physical origins of the TFR, the widely-accepted model assumes the mass distribution is spherically symmetric and governed by Newtonian dynamics on galactic scales. In this case, the centrifugal acceleration on an object moving in a circle of radius r is equal to the gravitational acceleration on the same object attributed to the mass inside a sphere of radius r :

$$V_{\text{rot}}^2 \propto \frac{M(r)}{r} \quad (2)$$

If the mass-to-light ratio and mean surface brightness for spirals are constant, then the above equation can be

rewritten as

$$L \propto V_{\text{rot}}^4 \quad (3)$$

While Aaronson et al. (1979) reproduced this relation with the infrared TFR, many other studies have empirically derived a power-law exponent of this relation deviating from 4 (see, for example, Sandage & Tammann 1976; Burstein 1982; Bottinelli et al. 1983; Pierce & Tully 1988), which is usually attributed to the complication in the stellar-halo mass relation (Mould 2020).

Tully-Fisher studies typically use either 21 cm H I line profiles or the H α emission line to construct the maximum rotational velocities of spiral galaxies. H I profiles provide perhaps the most direct way of measuring the maximum rotational velocity of a galaxy, provided the galaxy contains a sufficient amount of neutral hydrogen. At visible (rest-frame) wavelengths, the H α emission line is the most prominent and easily measurable line, making it the obvious choice to trace the rotational velocity of a spiral galaxy. However, it is more challenging to measure the maximum rotational velocity with H α , since observations must be made “far enough” from the galactic center for the rotation curve to flatten (Sofue & Rubin 2001). Moreover, the H α surface brightness tends to decrease more rapidly with galactocentric radius than H I and may be weak at radii where the rotational velocity flattens.

Once the rotational velocity of a galaxy is measured, the TFR can be used to estimate the luminosity, or absolute magnitude, of the galaxy. The absolute magnitude can then be compared to the apparent magnitude of the galaxy to determine its distance modulus.

3. DARK ENERGY SPECTROSCOPIC INSTRUMENT

The Dark Energy Spectroscopic Instrument (DESI; DESI Collaboration et al. 2022) is a multi-object fiber spectrograph designed to conduct a large-scale redshift survey covering at least 14,000 sq. deg. of the sky. DESI’s primary science goal is to determine the nature of dark energy by making the most precise measurement of the Universe’s expansion history to date (Levi et al. 2013). The instrument is installed on the Mayall 4-meter telescope at Kitt Peak National Observatory. The robotic fibers of DESI can measure up to 5,000 spectra, covering a wavelength range from 3600 Å to 9800 Å, over $\sim 8 \text{ deg}^2$ in a single exposure (DESI Collaboration et al. 2016a; Silber et al. 2023; Miller et al. 2024; Poppett et al. 2024), allowing the instrument to measure ~ 40 million redshifts over the 5-year survey (DESI Collaboration et al. 2016b). The layout of the focal plane allows each fiber to move within a patrol radius that has minimal overlap with neighboring fibers.

Spectroscopic targets for DESI are selected from the DESI Legacy Imaging Surveys (LS; [Dey et al. 2019](#)) using the DESI target selection pipeline ([Myers et al. 2023](#)). The targets are observed in tiles in a method following the optimized survey operations pipeline described in [Schlafly et al. \(2023\)](#). Redshifts are extracted in an offline spectroscopic pipeline using spectra measured in each fiber with the Redrock³⁸ template-matching software after being processed by the spectroscopic reduction pipeline ([Guy et al. 2023](#)).

This analysis uses spectroscopic observations made during DESI’s Survey Validation period (SV; [DESI Collaboration et al. 2024b](#)), the data from which comprise the DESI Early Data Release (EDR; [DESI Collaboration et al. 2024a](#)); to date, DESI has also released its first year of data ([DESI Collaboration et al. 2025a](#)). The last phase of SV consisted of a reduced version of the full DESI survey, covering 1% of the final 5-year DESI survey footprint. These observations were conducted in a series of rosettes on the sky using the final target selection algorithms and exposures of a depth typical of the main survey. For more details, see [DESI Collaboration et al. \(2024b\)](#).

As the main objective of DESI is to map the expansion history of the universe using Baryonic Accoustic Oscillations (BAO; [DESI Collaboration et al. 2024c, 2025b](#)), it has devised suitable target classes/tracers for the main survey: Bright Galaxies (BGS; [Hahn et al. 2023](#)), Luminous Red Galaxies (LRG; [Zhou et al. 2023](#)), Emission Line Galaxies (ELG; [Raichoor et al. 2023](#)), and Quasi-Stellar Objects (QSO; [Chaussidon et al. 2023](#)), as well as Milky Way stars (MWS; [Cooper et al. 2023](#)). In addition to these primary target classes, DESI also carries out various secondary targeting programs using spare fibers ([Myers et al. 2023](#)) to further increase the scientific value and targeting efficiency of the survey. One of these programs is the DESI Peculiar Velocity Survey ([Saulder et al. 2023](#)).

3.1. The DESI Peculiar Velocity Survey

The DESI Peculiar Velocity (PV) Survey ([Saulder et al. 2023](#)) is designed to measure the peculiar motions of local galaxies up to a redshift of 0.15 and thereby improve cosmological constraints on $f\sigma_8$, the product of the redshift-dependent growth rate of structure (f) and the amplitude of the linear power spectrum on the scale of $8 h^{-1}$ Mpc (σ_8). In addition to spectroscopic redshifts, redshift-independent distance indicators are also required to derive peculiar motions. To this end, the DESI PV Survey targets suitable galaxies that can

be used for either the Fundamental Plane (early-type galaxies) or the Tully-Fisher relation (late-type galaxies). The target design of the DESI PV Survey is described in [Saulder et al. \(2023\)](#). Here, we focus on the Tully-Fisher sample; see [Said et al. \(2025\)](#) for a discussion of the Fundamental Plane sample and its calibration.

For the late-type galaxies used in the TFR, we select galaxies that are in the size-limited Siena Galaxy Atlas 2020 ([Moustakas et al. 2023](#)), built with the DESI Legacy Imaging Surveys DR9 ([Dey et al. 2019](#)) north of -30° declination. The SGA-2020 is comprised of galaxies with diameters of the 25th magnitude arcsec^{-2} isophote, $D(25)$, greater than $20''$. To be included in the TFR sample, the SGA-2020 galaxy’s photometric profile must have a Sersic index of less than 2 (characteristic of spiral galaxies; [Blanton & Moustakas 2009](#)); and its inclination angle must be greater than 25° to ensure both a sufficient fraction of the galaxy’s rotational velocity along the line of sight and a confident alignment of the galaxy’s position angle with its major axis. The distribution of TF galaxies on the sky is shown in [Fig. 1](#). For each of the galaxies in the TFR sample in DESI SV, we position fibers at both the galactic center and at $0.33R_{26}$ on either side of the center along the major axis, where R_{26} is the radius of the 26 mag arcsec^{-2} r -band isophote. As described in [Saulder et al. \(2023\)](#), the rotational velocities were measured at $0.33R_{26}$ in the DESI PV Survey during DESI SV, as this was thought to be the furthest angular distance from the galaxies’ centers where we could still reliably measure the redshift. As discussed in [Saulder et al. \(2023\)](#), the SV observations showed that we could increase the radius of the fiber positions slightly, so the fibers are placed at $0.4R_{26}$ in the DESI main survey.

3.2. Photometric corrections

To adjust for various influences on the magnitudes of the galaxies, we apply a series of corrections to the photometry and compute a corrected apparent magnitude:

$$m_{r,\text{corr}} = m_r - A_{\text{MW dust}} - A_{\text{internal dust}} + A_k + A_{\text{sys}} \quad (4)$$

where m_r is the magnitude measured in the r -band within the 26-mag isophote (as given in the SGA-2020), $A_{\text{MW dust}}$ corrects for dust extinction in the Milky Way, $A_{\text{internal dust}}$ corrects for dust extinction internal to the galaxy, A_k is the k -correction, and A_{sys} corrects for the systematic offset between the two photometric surveys used in this analysis.

We correct for the extinction due to dust in the Milky Way’s interstellar medium (ISM) using the $E(B - V)$ map derived from $g - r$ using DESI MWS spectra ([Zhou](#)

³⁸ <https://github.com/desihub/redrock>.

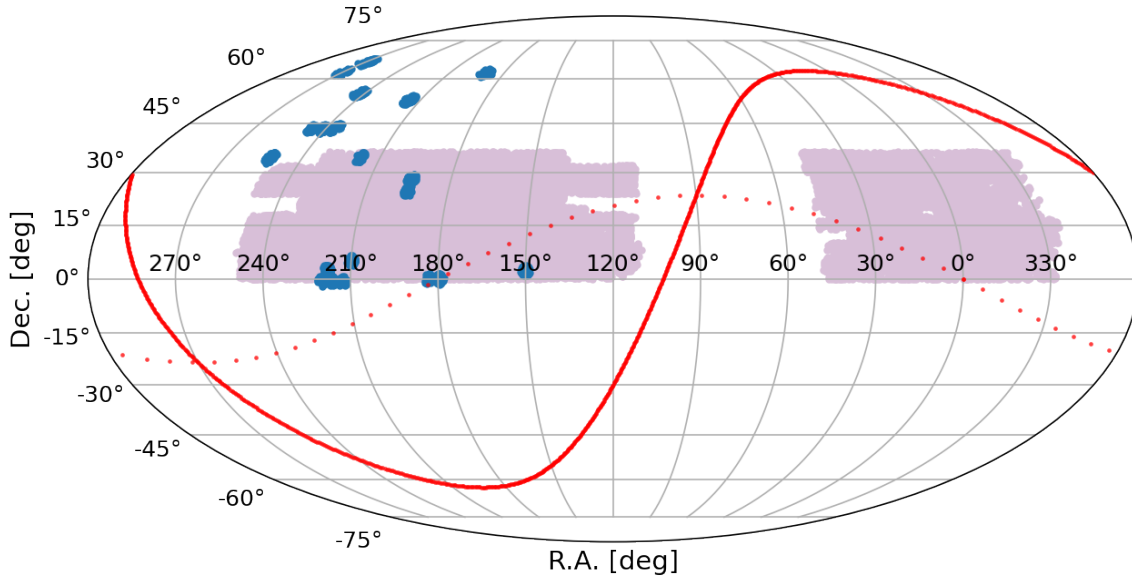


Figure 1. The distribution of Tully Fisher galaxies within the DESI EDR dataset, presented here in a Mollweide projection. The purple shaded region corresponds to the ALFALFA (Haynes et al. 2018) footprint, and the red solid line represents the plane of the Milky Way.

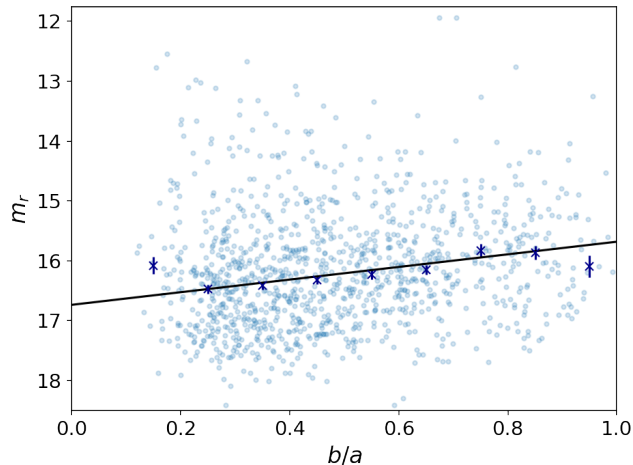


Figure 2. Observed correlation between r -band apparent magnitude and axis ratio. A linear fit to the median magnitudes in each bin (dark blue crosses) is shown in the black line.

et al. 2024). The magnitude correction is computed as

$$A_{\text{MW dust}} = R_r E(B - V), \quad (5)$$

where $R_r = 2.165$ is the ratio of total to selective extinction in the r -band through an airmass of 1.3 for a 7000 K spectrum, as discussed in Zhou et al. (2024).

Galaxies viewed at higher inclination angles will be subject to internal dust extinction, with the amount of extinction a function of both the galaxy’s dust content and the inclination angle. To correct for this extinction,

we fit for and remove the residual correlation between the galaxy’s r -band magnitude and axis ratio, shown in Fig. 2. We correct all galaxies so that:

$$A_{\text{internal dust}} = d \left(\frac{b}{a} - 1 \right) \quad (6)$$

where $d = -1.05^{+0.18}_{-0.19}$ is the slope of the line fit to the median magnitudes binned by the axis ratio.

The photometry used in this analysis comes from the LS, where images above $\text{Dec} \geq +32.375^\circ$ are from the Beijing-Arizona Sky Survey (BASS; Zou et al. 2017), conducted at the Bok 2.3 m telescope at the Kitt Peak National Observatory (KPNO) in Arizona, and the Mayall z -band Legacy Survey (MzLS; Dey et al. 2019), conducted at the Mayall 4-m telescope at KPNO, and images below this declination were obtained using the Dark Energy Camera (DECam; Flaugher et al. 2015) at the 4 m Blanco telescope at the Cerro Tololo Inter-American Observatory in Chile. Due to the use of different telescopes, cameras, and filters between the BASS and DECam LS (DECaLS) imaging, there are zero-point calibration variations between them; see Sec. 7.2 of Dey et al. (2019) for details. With the overlap region of the two imaging surveys, we can correct for these systematic variations: as described in the FP analysis (Said et al. 2025), it was shown that

$$m_{r,\text{BASS}} - m_{r,\text{DECaLS}} = 0.0234 \quad (7)$$

with a root mean square (RMS) deviation of 0.02 mag and an error on the mean of 0.0005 mag. As in Said

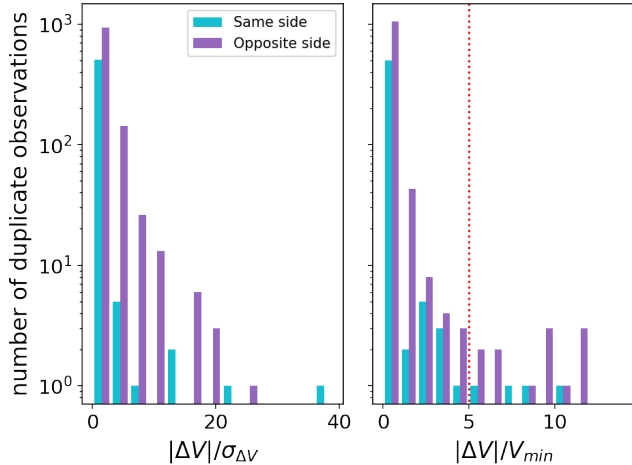


Figure 3. *Left:* Pull distribution of the difference in velocity observed at $0.33R_{26}$ for multiple observations on the same galaxy (on the same side of the galactic center in teal, opposite sides in purple). *Right:* Distribution of $|\Delta V|/V_{\min}$ for galaxies with multiple observations at $0.33R_{26}$. All observations on a galaxy must fall to the left of the dotted red line to be in the final sample. Note that the y -axis uses log scaling to show the tails of the distributions.

et al. (2025), we adjust the northern r -band magnitudes by 0.0234 to account for this offset.

Finally, we apply K -corrections to the photometry with the `kcorrect` Python package (Blanton & Roweis 2007) to account for observing slightly different parts of a galaxy’s SED due to its redshift. We K -correct to a redshift of 0.05, the median redshift of our galaxy sample, to minimize this correction as much as possible.

4. MEASURING THE ROTATIONAL VELOCITY

We measure the rotational velocity of a galaxy by comparing the observed redshift of the galaxy’s center, giving its systemic motion, and at a point along its major axis, which comprises both its systemic motion and the component of the rotational motion along the line of sight at that location in the galaxy:

$$\frac{V}{c} = \frac{1+z}{1+z_{\text{center}}} - 1 \quad (8)$$

To each redshift uncertainty reported by Redrock, we add in quadrature a 7 km/s uncertainty to account for Redrock’s precision uncertainty. As described in Lan et al. (2023), this was quantified with repeat observations conducted during DESI SV; we use the value measured for Redrock’s success on ELG spectra because our spectra primarily contain emission lines.

As mentioned in Sec. 2, the TFR is frequently constructed using H I velocities, since the slowly decreasing surface brightness of H I as a function of galactocentric radius makes it possible to measure H I velocities

in the “flattened” part of the galactic rotation curve. However, as shown in Yegorova & Salucci (2007), it is possible to calibrate the TFR at any galactocentric radius, so long as one is careful to only apply the TFR to observations made at this same radius. The scatter in the calibrated TFR also decreases with increasing radius (Yegorova & Salucci 2007), since more of the galaxies will have reached their asymptotic velocity, so it is desirable to calibrate with as large of a radius as possible.

In DESI observations, we apply several quality selection criteria. We require all galaxy center observations to have Redrock redshifts with `DELTA CHI2` > 25 (the difference in the χ^2 of Redrock’s best-fit and second-best-fit spectrum model) and `ZWARN` = 0 (a Redrock fitting flag; 0 = good).

For off-center observations, we do not require the same Redrock quality criteria as for the center observations because the S/N of the off-center spectra will necessarily be worse than the center spectra. Instead, we require the calculated rotational velocity to be between 10–1000 km/s and that all rotational velocities with `DELTA CHI2` > 25 at $0.33R_{26}$ satisfy $|\Delta V|/V_{\min} < 5$, where ΔV is the difference in rotational velocity between any two observations at that radius, and V_{\min} is the minimum velocity measured at that radius. A limit of 5 on this ratio was selected based on visual inspection of the spectra and Redrock redshifts for those galaxies with multiple observations at $0.33R_{26}$.

The pull distribution for $|\Delta V|$ is shown on the left in Fig. 3, and the distribution of $|\Delta V|/V_{\min}$ is shown on the right in Fig. 3; for both, we separate the duplicate observations based on whether they are taken from the same side of the galaxy or opposite sides of the galactic center. The uncertainty on ΔV , $\sigma_{\Delta V}$, is the quadrature sum of the two velocities being compared: $\sigma_{\Delta V}^2 = \sigma_{V_1}^2 + \sigma_{V_2}^2$ for $\Delta V = V_1 - V_2$. We find a wider pull distribution for observations made on opposite sides of the galactic center, which we primarily attribute to the center observation being slightly off from the kinematic center of the galaxy. A detailed kinematic map of the galaxy is required to correct for this potential systematic effect, which is unavailable to us in this analysis. This systematic effect contributes to, and is therefore accounted by, the scatter in the calibrated TFR.

We adjust each measured velocity with the photometric inclination angle to estimate the total rotational velocity at that particular orbital radius in the galaxy:

$$V_{\text{rot}} = \frac{V}{\sin i} \quad (9)$$

where

$$\cos^2 i = \frac{(b/a)^2 - q_0^2}{1 - q_0^2}, \quad (10)$$

b/a is the photometric axis ratio from the SGA-2020, with $q_0 = 0.2$ (Tully & Pierce 2000).

4.1. Rotational velocity systematics

To assess the systematics associated with measuring the rotational velocity at this galactocentric radius, we compare the measured rotational velocities at $0.33R_{26}$ in the DESI PV Survey with the expected rotational velocity at $0.33R_{26}$ inferred from the SDSS Mapping Nearby Galaxies at APO Survey (MaNGA Bundy et al. 2015) for the same galaxies. The comparison of the 55 galaxies that are in both samples is provided below.

4.1.1. SDSS MaNGA

Ravi et al. (2024) model the $H\alpha$ velocity maps of ~ 5500 galaxies from the SDSS MaNGA DR17 (Abdurro'uf et al. 2022). MaNGA used a bundle of spectroscopic fibers (an IFU containing between 19 and 127 fibers) to observe galaxies out to $1.5R_e$ or $2.5R_e$ of $\sim 10,000$ galaxies (Drory et al. 2015). The light from the IFUs was received by two dual-fed spectrographs covering a wavelength range of 3600–10,300 Å with a resolution $\lambda/\Delta\lambda \sim 2000$ (Smee et al. 2013).

Ravi et al. (2024) fit the $H\alpha$ velocity field using the parameterization

$$V(r) = \frac{V_{\max}r}{(R_{\text{turn}}^\alpha + r^\alpha)^{1/\alpha}}, \quad (11)$$

where $V(r)$ is the tangential rotational velocity at galactocentric radius r , V_{\max} is the maximum velocity of the rotation curve, R_{turn} is the radius at which the rotation curve pivots from increasing to flat, and α is a measure of how quickly the rotation curve transitions from increasing to flat (Barrera-Ballesteros et al. 2018). During the fitting procedure, the following parameters are allowed to vary: V_{\max} , R_{turn} , α , the kinematic center of the galaxy, the inclination angle i of the galaxy, and the position angle ϕ of the galaxy (the angle east of north of the major axis). For more details about the modeling of the velocity fields, see Ravi et al. (2024).

4.1.2. Kinematic *v.* photometric rotation angle

We check how our rotational velocity at $0.33R_{26}$ is affected by an incorrect position angle for the galaxy. As described in Saulder et al. (2023), the DESI fibers are placed at $0.33R_{26}$ from the galactic center along the major axis of the galaxy; we assume that the galaxy's major axis is at a position angle ϕ east of north, where ϕ is provided by the SGA-2020 and was derived from photometry. If there is a mismatch between the photometric and kinematic position angles, then the rotational velocity that we calculate in Eqn. 9 needs an additional correction.

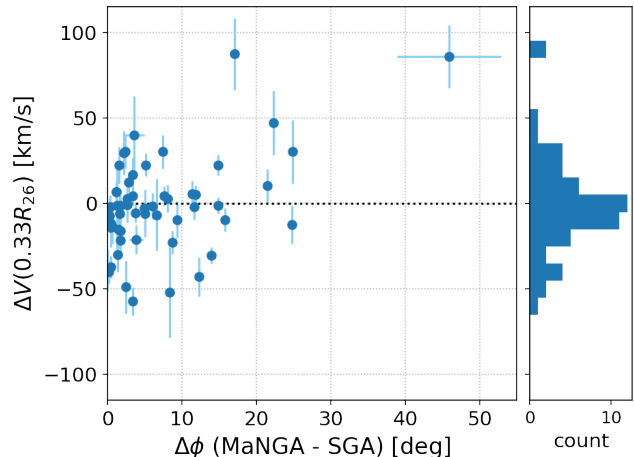


Figure 4. Difference between the velocity measured at $0.33R_{26}$ from the DESI PV Survey (this work) and the rotational velocity at $0.33R_{26}$ expected from the fits by Ravi et al. (2024) as a function of the difference in position angle, $\Delta\phi$, between the SGA-2020 (used for targeting in the DESI PV Survey) and the fitted rotation angle from Ravi et al. (2024). The black dotted line denotes a velocity difference of zero.

To test the effect of a difference between the position angles on the measured velocity, we compare $\Delta V(0.33R_{26})$, the difference between the rotational velocity measured at $0.33R_{26}$ in the DESI PV Survey and the rotational velocity at the same radius predicted by the fit by Ravi et al. (2024), with $\Delta\phi$, the difference between position angles from the SGA-2020 and that fit by Ravi et al. (2024). As shown in Fig. 4, we find no relationship between the velocity difference and the rotation angle offset. The SDSS MaNGA DR17 $H\alpha$ velocity maps of the two outliers with $\Delta V(0.33R_{26})$ around 100 km/s show significant spaxel noise beyond the central regions of the galaxies; while the observed DESI rotational velocities differ greatly from that predicted by the best-fit rotation curve of Ravi et al. (2024), they are consistent with the spaxel scatter at $0.33R_{26}$ for both of these galaxies.

4.1.3. Scatter in DESI Rotational Velocities

To quantify the scatter introduced by the measurement of the rotational velocity at $0.33R_{26}$, versus versus fully sampling the galaxy's velocity field as in SDSS MaNGA, we compare the DESI rotational velocity measurements at $0.33R_{26}$ to the predicted velocity from the rotation curve fits of Ravi et al. (2024).

To measure just the effect that our observations have on the measured velocity, we convert the predicted rotational velocity from the SDSS MaNGA fits to the SGA-2020 “frame” to account for differences in the po-

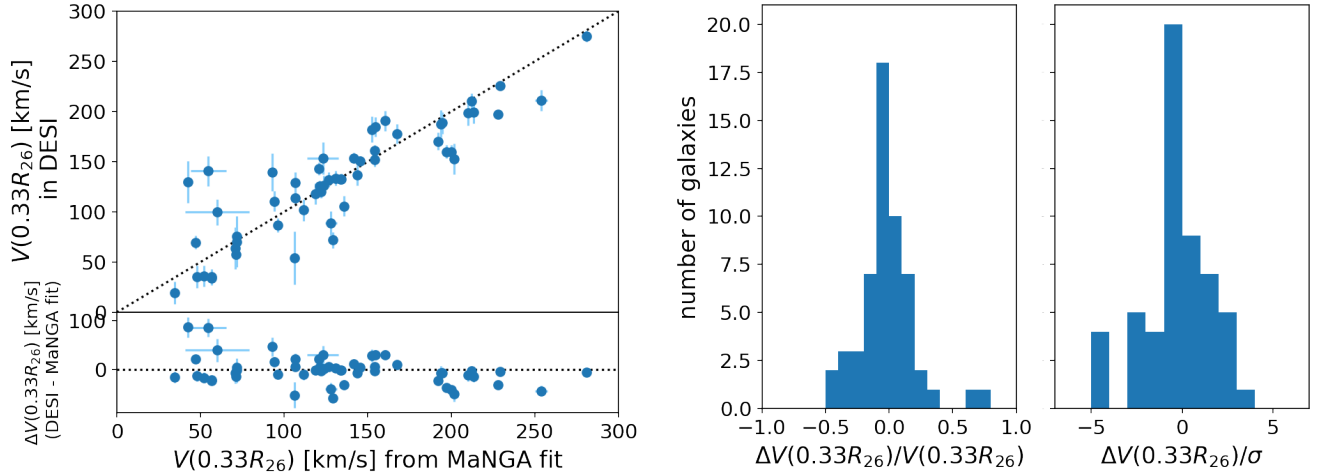


Figure 5. *Left:* Comparison between the rotational velocity at $0.33R_{26}$ observed in the DESI PV Survey and expected from the SDSS MaNGA DR17 rotation curve fits of Ravi et al. (2024), corrected for differences in position angle and inclination. The black dotted line denotes equality between the two velocities. *Center:* Distribution of the perpendicular distance to $y = x$ normalized by the corresponding value on $y = x$ for each of the galaxies appearing in the left-hand plot. *Right:* Pull distribution of $\Delta V(0.33R_{26})$.

sition and inclination angles. The conversion from the SDSS MaNGA “frame” (defined by the best-fit values of Ravi et al. 2024) to the SGA-2020 “frame” is

$$V_{\text{MaNGA, expected}} = A(Q \sin i)B(\Delta\phi)V_{\text{MaNGA}}, \quad (12)$$

where

$$A(Q \sin i) = \frac{\sin i_{\text{MaNGA}}}{\sin i_{\text{SGA}}}, \quad (13)$$

and

$$B(\Delta\phi) = \cos(|\phi_{\text{MaNGA}} - \phi_{\text{SGA}}|). \quad (14)$$

Here, quantities with a subscript “MaNGA” refer to the best-fit values reported by Ravi et al. (2024), while quantities with the subscript “SGA” correspond to the photometric values reported in the SGA-2020. These corrections transform the calculated rotational velocity so that $V_{\text{MaNGA, expected}}$ corresponds to the rotational velocity that we would expect to observe at $0.33R_{26}$ if the best-fit rotation curve derived by Ravi et al. (2024) describes the galaxy when it is oriented as defined by the photometric parameters of the SGA-2020; this conversion does not affect the uncertainty in $V_{\text{MaNGA, expected}}$.

The comparison of our measured velocities at $0.33R_{26}$ with those expected from the SDSS MaNGA rotation curve fits is shown on the left in Fig. 5. The DESI observations recover the expected rotational velocity at $0.33R_{26}$, albeit with additional scatter. To quantify the scatter in this correlation, we calculate the perpendicular distance to the line of equality ($y = x$). The distribution of these distances, normalized by the position on $y = x$ that was used to calculate this distance, is shown in the center panel in Fig. 5. The standard deviation of

this distribution is 22%, which will be a component of the intrinsic scatter that we measure in our calibrated TFR.

5. CALIBRATING THE TULLY-FISHER RELATION

The TFR, shown in Eqn. 3, is commonly written in the form

$$M_r = a \log \left(\frac{V}{V_0} \right) + b \quad (15)$$

where M_r is the absolute magnitude of the galaxy (in this work, in the r -band), a is slope that corresponds to the power-law exponent of the relation, b is the zero-point of the relation, and $\log(V_0[\text{km/s}]) = 2.01$ is the median $\log V$ of all galaxies used to calibrate the TFR. We use a non-zero value for $\log V_0$ to shift the relation to minimize the correlation between the calibrated slope and y -intercepts of the TFR. Calibrating the TFR involves determining both the slope and zero-point of the relation. We follow a modification of the calibration scheme used in Kourkchi et al. (2020a), where the slope is calibrated using galaxies in the same cluster and those with independently-measured distances, and the zero-point is found using the galaxies with independently-measured distances.

We require all galaxies used to calibrate either the slope or zero-point to have a minimum inclination angle of 45° ; this is a tighter constraint than what we require for inclusion in the TF sample, to increase the robustness of our calibration. We also visually inspect all calibration galaxies to ensure that there is no contamination from bright stars and/or overlapping galax-

ies. For galaxies with observed rotational velocities on both sides of the galactic center, we use the weighted average of the absolute value of the two velocities.

Dwarf galaxies (defined as those fainter than the line perpendicular to the calibrated TFR, intersecting the calibrated TFR at $M_r = -17$) are not included in the calibration of the TFR, as both their photometry and rotational velocities are typically less reliable than their brighter counterparts, and because they are known to have a significantly higher gas mass fraction than brighter galaxies. The difference in mass fraction violates the assumption of the TFR that all galaxies have a uniform mass-to-light ratio. We therefore remove dwarf galaxies from our TFR calibration. However, because the slope of the calibrated TFR is not known until after calibration is complete, their removal requires an iterative process. We first fit for the slope and zero-point of the TFR using all available cluster galaxies. We then calculate and remove any galaxies with absolute magnitudes fainter than the dwarf limit based on this calibration, and we refit for the slope and zero-point of the TFR with this reduced galaxy sample. We repeat this process until the galaxies considered to be dwarfs (i.e. below the line perpendicular to the latest calibration of the TFR that passes through $M_r = -17$) does not change with the latest calibration. Here, we report the final values of the calibrated slope and zero-point after this iterative process converges.

5.1. Defining cluster membership

We use the Coma Cluster to calibrate the slope of the TFR for the DESI EDR, as it was the only cluster with a significant number of members observed during DESI SV. Since the members of the Coma Cluster are all approximately the same distance from us, their scatter in the TFR is only due to the intrinsic scatter of the TFR. Otherwise, they should all follow the same slope of the TFR for rotational velocities measured at the same galactocentric radius.

Similar to Kourkchi et al. (2020a), we define galaxies in the Coma Cluster as those with either

$$R_p < 1.5R_{2t} \quad \text{and} \quad v < V_c \pm 3\sigma_v \quad (16)$$

$$1.5R_{2t} \leq R_p \leq 3R_{2t} \quad \text{and} \quad v < V_c \pm 2\sigma_v \quad (17)$$

where R_p is the galaxy's projected distance from the center of the Coma Cluster, $R_{2t} = 2.129$ Mpc (Tully 2015) is the Coma Cluster's projected second turnaround radius, $\sigma_v = 886$ km/s (Tully 2015) is the Coma Cluster's velocity dispersion (calculated from the bi-weighted line-of-sight velocities of its group members), and $V_c = 7176$ km/s is the average radial velocity of the Coma Cluster in the CMB frame (computed from the clus-

ter's distance modulus from Tully 2015). The limits of Eqn. 16 are depicted by the blue dotted lines in Fig. 6, with Eqn. 17 shown with the solid blue lines.

After the inclination cut and visual inspection, we are left with 41 galaxies in the Coma Cluster with which we can fit for the TFR slope. The α , δ , and redshifts of these galaxies are shown in Fig. 6 and reported in Table 1.

5.2. Zero-point calibrators

To calibrate the zero-point of the TFR, we use galaxies observed as part of the DESI PV Survey that have distances in the Extragalactic Distance Database (EDD; Tully et al. 2009). Of the 11 galaxies observed in the DESI PV Survey EDR with independent distance measurements from the EDD, only two of them satisfy the quality criteria described in Sec. 5. Both their distances are calibrated from Type Ia SNe, with distance moduli measured by Stahl et al. (2021). Using the distance moduli, μ , we compute the absolute magnitudes of these galaxies in the r -band:

$$M_r = m_r - \mu \quad (18)$$

The α , δ , and redshifts of these two galaxies are reported in Table 2.

5.3. Joint calibration of the slope and zero-point

We perform a joint fit of galaxies in the Coma Cluster and those with independent distances to calibrate the TFR, requiring both populations to have the same slope. The fit to the population with independent distances is used to fix the TFR zero point, while the y -intercept for the Coma cluster is treated as a nuisance parameter. We subclass the HyperFit³⁹ package (Robotham & Obreschkow 2015) to perform the fit so that we can quantify the scatter in the TFR. HyperFit minimizes the distance perpendicular to the best-fit line, so we are fitting a hybrid of both the TFR and inverse TFR:

$$a \log \left(\frac{V}{V_0} \right) = m_r - b_{\text{Coma}} = M_r - b_{\text{opt}} \quad (19)$$

where our free parameters are a , b_{Coma} , and b_{opt} . Hyperfit also quantifies the residual scatter along the vertical (magnitude) axis, σ_{Coma} , based on the best fit.

As the SGA-2020 is size-limited, our calibration sample contains a Malmquist-like bias (with size instead of flux). To account for this, we weight each galaxy in the fit by the maximum volume within which it could be included within the SGA-2020. To remove any effect this

³⁹ Available at <https://github.com/CullanHowlett/HyperFit>

Table 1. Coma cluster galaxies used for TFR slope calibration

SGA-2020 ID	R.A. [deg]	Decl. [deg]	Redshift	$D(26)$ [arcmin]	$m_r(26)$ [AB mag]	$V(0.33R_{26})$ [km/s]
25532	195.976671	28.310624	0.02673(2)	0.79	16.91 ± 0.006	46.5 ± 7.2
98934	194.206914	27.093896	0.02315(1)	1.40	14.38 ± 0.011	188 ± 13
122260	195.847744	27.306878	0.01857(2)	0.45	17.30 ± 0.018	65.2 ± 8.7
191275	194.575941	27.848483	0.02534(4)	0.68	16.74 ± 0.026	20 ± 24
196592	193.638307	27.632752	0.02439(2)	1.49	14.45 ± 0.023	153 ± 16
202666	195.212967	27.742984	0.02712(5)	0.76	16.44 ± 0.011	56 ± 19
221178	193.067420	27.533159	0.01843(1)	1.02	15.24 ± 0.005	81.8 ± 8.3
291879	195.433257	28.999533	0.02153(3)	1.40	14.73 ± 0.018	114 ± 13
309306	193.526516	29.242659	0.02465(5)	0.97	16.03 ± 0.016	119 ± 42
337817	194.168156	28.217658	0.02773(2)	0.61	16.64 ± 0.037	151 ± 24
364410	193.281401	28.241242	0.02346(2)	0.63	17.01 ± 0.020	55.5 ± 7.1
364929	194.213359	29.378171	0.02391(4)	1.38	14.98 ± 0.005	67 ± 17
365429	194.181327	27.034746	0.01869(3)	0.70	15.46 ± 0.029	73 ± 27
366393	194.661188	27.013210	0.02340(2)	0.69	16.87 ± 0.013	77.0 ± 5.9
378842	194.270257	28.209628	0.01718(2)	0.43	17.64 ± 0.006	49.6 ± 8.0
455486	196.088608	24.430244	0.02514(2)	1.12	16.28 ± 0.027	66.9 ± 7.3
465951	196.148924	28.627694	0.02239(2)	0.62	15.48 ± 0.006	55 ± 12
479267	193.223264	28.371257	0.02358(2)	2.09	13.43 ± 0.012	260.6 ± 5.4
486394	193.975798	23.802604	0.01904(2)	0.81	16.48 ± 0.031	69.1 ± 7.0
566771	194.666055	26.759415	0.02486(2)	1.05	16.21 ± 0.021	57.9 ± 9.9
645151	195.130309	28.950469	0.02334(2)	1.10	16.31 ± 0.028	102.3 ± 7.2
747077	194.538607	28.708611	0.02542(2)	2.30	14.35 ± 0.014	138.1 ± 9.8
748600	193.655970	27.691999	0.02825(3)	0.62	15.77 ± 0.048	107 ± 14
753474	195.164866	29.019325	0.02427(3)	2.38	13.52 ± 0.006	197.7 ± 7.4
819754	194.119091	27.291300	0.02508(2)	1.13	14.77 ± 0.005	112.5 ± 6.9
826543	195.188419	27.747018	0.03111(8)	0.68	17.47 ± 0.013	112 ± 31
841705	195.960413	28.054375	0.02102(3)	0.70	15.81 ± 0.032	87 ± 14
917608	193.444254	27.385853	0.02765(1)	0.77	16.35 ± 0.007	105 ± 12
995924	194.348213	27.549951	0.02019(6)	0.46	16.96 ± 0.016	45 ± 20
1050173	195.038059	27.866433	0.01775(2)	0.52	15.38 ± 0.016	114 ± 13
1167691	193.464618	28.979424	0.02649(2)	1.10	14.86 ± 0.017	139.9 ± 6.9
1203610	195.313399	27.669224	0.02360(3)	0.78	16.09 ± 0.024	63 ± 22
1203786	194.431835	29.003335	0.02313(2)	0.72	17.18 ± 0.038	61.0 ± 6.2
1269260	194.802578	25.003968	0.02589(3)	0.53	17.18 ± 0.014	52 ± 10
1274409	193.474729	28.186669	0.02561(2)	0.88	15.39 ± 0.017	129 ± 11
1284002	193.480767	28.393845	0.02467(3)	0.97	16.62 ± 0.008	244 ± 18
1323268	195.158001	28.057463	0.02578(2)	1.11	14.65 ± 0.008	127.3 ± 7.7
1356626	195.093287	27.623562	0.02537(4)	0.52	16.36 ± 0.028	68 ± 25
1364394	194.819484	27.106093	0.02804(1)	0.52	15.95 ± 0.014	153.7 ± 5.4
1379275	195.449906	27.354792	0.02026(5)	0.68	16.82 ± 0.009	83 ± 32
1387991	196.019819	27.850501	0.02129(3)	0.73	15.97 ± 0.034	125 ± 14

NOTE—List of the 41 galaxies in the Coma cluster used for calibrating the slope of the TFR. Sky positions and diameters of the 26 mag arcsec⁻² isophote in the r -band are from the SGA-2020 (Moustakas et al. 2023). Redshifts are measured from the DESI EDR spectra, and rotational velocities at $0.33R_{26}$ are computed as described in Sec. 4.

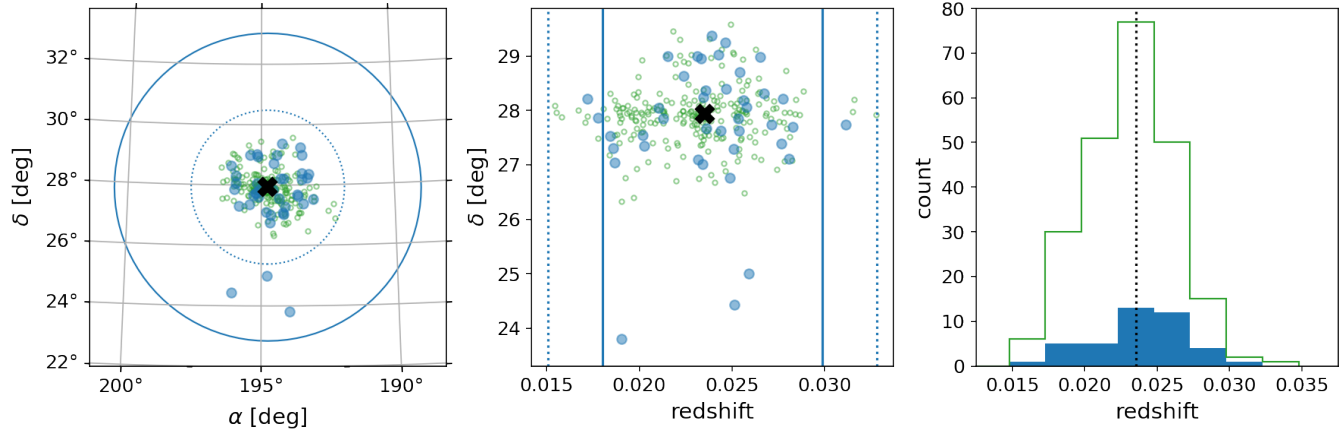


Figure 6. The distribution in α , δ , and redshift of Coma Cluster galaxies used in this analysis, shown in blue. Galaxies within the Coma Cluster used in the complementary Fundamental Plane analysis by Said et al. (2025) are shown in green. The center of the Coma Cluster is denoted by the black X in the first two panels and the dotted vertical line in the third. Galaxies must fall within the blue dashed lines (Eqn. 16) or blue solid lines (Eqn. 17) to be assigned to the cluster.

Table 2. Galaxies used for TFR zero-point calibration

SGA-2020 ID	R.A. [deg]	Decl. [deg]	Redshift	$D(26)$ [arcmin]	$m_r(26)$ [AB mag]	$V(0.33R_{26})$ [km/s]	μ [mag]	SN
294387	183.547194	-0.831611	0.02486(2)	1.22	14.95 ± 0.005	135.7 ± 6.0	34.77 ± 0.30	SN2019kcx
464075	242.480987	43.129126	0.03283(3)	1.88	14.06 ± 0.016	247.4 ± 3.6	35.56 ± 0.16	2006cc

NOTE—List of the two galaxies used for calibrating the zero-point of the TFR. Sky positions and diameters of the 26 mag arcsec⁻² isophote in the r -band are from the SGA-2020 (Moustakas et al. 2023). Redshifts are measured from the DESI EDR spectra, and rotational velocities at $0.33R_{26}$ are computed as described in Sec. 4. Distance moduli are from Stahl et al. (2021).

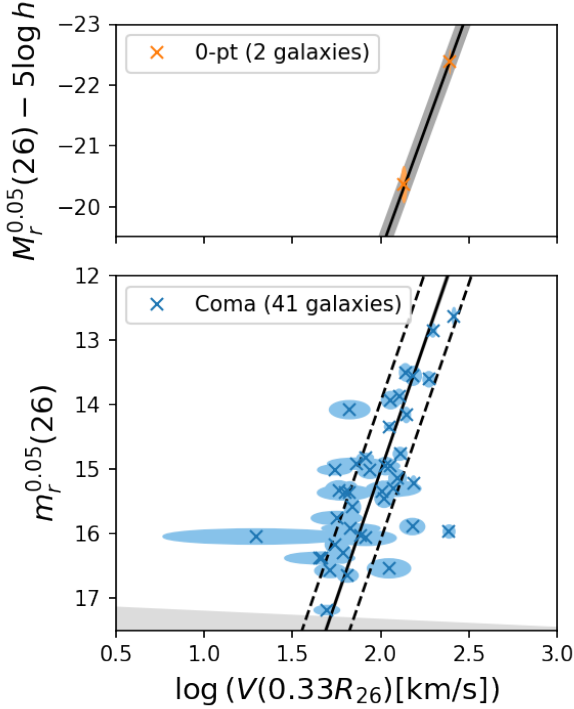


Figure 7. Calibrated TFR of the DESI EDR galaxies with $i > 45^\circ$ in the Coma Cluster (lower panel; blue points) and with independent distance measurements listed in the EDD (upper panel; orange points). The shaded gray region in the bottom panel denotes the region within which dwarf galaxies are defined. The calibrated TFR is drawn with the solid black line, and the dispersion of the points is shown with the black dashed lines.

normalization would have on the reported uncertainties, we normalize each weight by the volume within $z = 0.1$. Each galaxy’s weight is $f_{\max \text{ vol}}^{-1}$, where

$$f_{\max \text{ vol}} = \left(\frac{d_{\max}}{d(z = 0.1)} \right)^3 \quad (20)$$

where d_{\max} is the comoving distance at which the galaxy would have an angular diameter of $0.2'$ (the size limit of the SGA-2020), and $d(z = 0.1)$ is the comoving distance at $z = 0.1$.

Fig. 7 shows the TFR for our galaxies in the Coma Cluster (bottom panel) and for the two galaxies with independent distance measures (top panel), with the best-fit slope value of -7.96 ± 0.13 AB mag, a best-fit y -intercept value of 14.95 ± 0.02 AB mag for the Coma Cluster, and a best-fit 0-pt value of $-19.34^{+0.30}_{-0.29}$ AB mag. The residual scatter along the magnitude axis for the Coma Cluster is 1.07 ± 0.02 AB mag; from our comparison to the expected velocities from SDSS MaNGA (see Sec. 4.1.3), 0.74 AB mag of this can be attributed to measuring the rotational velocity at $0.33R_{26}$. The corner plot for the

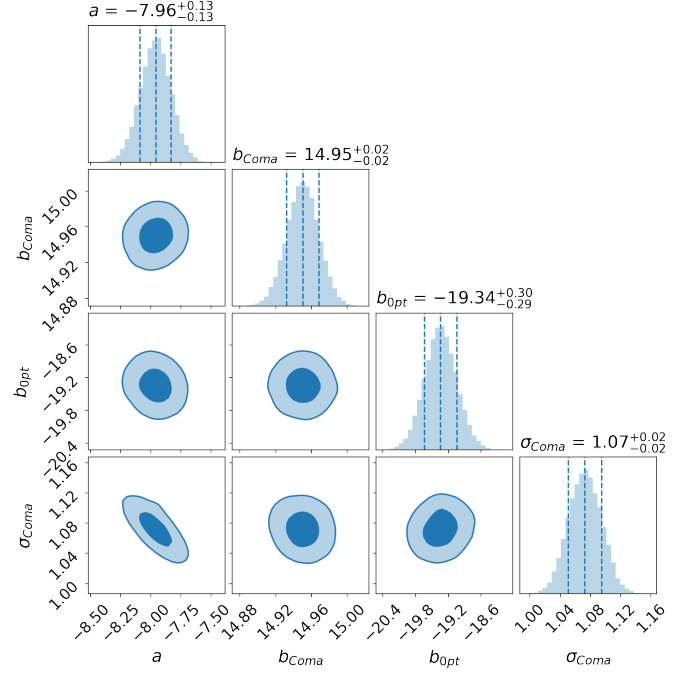


Figure 8. Corner plot of the linear fit to the Coma Cluster galaxies and galaxies with independent distances shown in Fig. 7, where a is the slope, b_{Coma} is the y -intercept of the Coma Cluster’s TFR, $b_{0\text{pt}}$ is the y -intercept of the galaxies with independent distances, and σ_{Coma} is the intrinsic scatter in the Coma Cluster along the magnitude axis.

TFR calibration is shown in Fig. 8. The two galaxies with apparent magnitudes between 16 and 17 that have higher velocities than expected relative to the rest of the cluster were looked at in detail to discern why they might be outliers: there does not appear to be any failure in deriving the photometric properties in the SGA-2020, nor do their spectra look unusual, so it is possible that these galaxies have higher velocities than anticipated because their rotation curves have plateaued.

6. MEASURING PECULIAR VELOCITIES

Using the calibrated slope and zero-point from Sec. 5, we calculate the distance to 1136 spiral galaxies, out of a total of 1163 spiral galaxies observed in the DESI PV Survey EDR; 27 are considered dwarf galaxies by our calibrated TFR, which we therefore exclude from our final sample. The TFR for all of these objects is shown in Fig. 9, where the absolute magnitudes for each object are calculated using the proper distance for a flat Λ CDM cosmology with $\Omega_M = 0.3151$, $H_0 = 100h$ km/s/Mpc, and the redshift is that of the center of the galaxy as observed with DESI. The vertical scatter between each galaxy and the calibrated TFR (shown in black) is a result of the peculiar motion of the galaxy along the line of sight and the intrinsic scatter of the TFR. We calculate

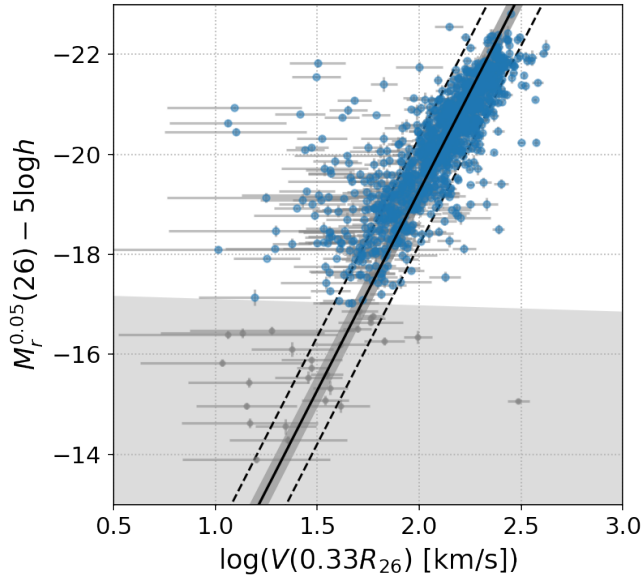


Figure 9. TFR for DESI PV Survey EDR galaxies. Our calibrated TFR is shown in the solid black line, with the light gray band representing the 1σ uncertainty around the calibrated TFR; the intrinsic dispersion of the calibrated TFR is shown with the black dashed lines. The gray shaded region towards the bottom denotes galaxies considered dwarfs by our calibration; those that fall within it are shown as small gray points. Vertical scatter is the result of the peculiar motion of each galaxy.

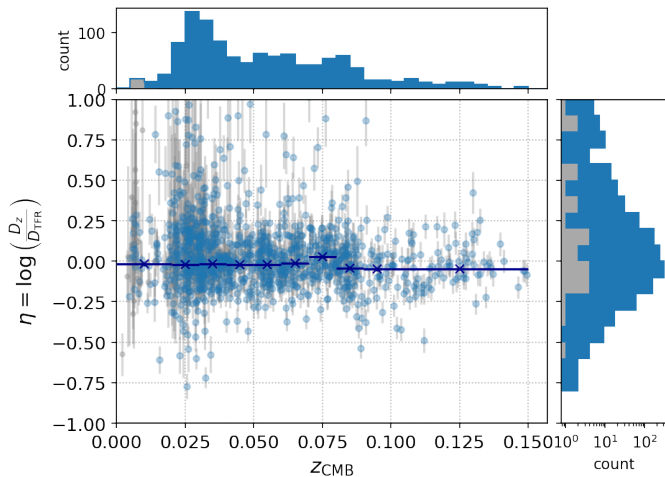


Figure 10. Log distance ratio as a function of redshift for the DESI PV Survey EDR galaxies in the TF sample. The average log distance ratio in redshift bins are shown in dark blue crosses. Galaxies considered to be dwarfs by our TFR (those whose rotational velocities give an absolute magnitude below the line perpendicular to the calibrated TFR at $M_r = -17$) are shown in gray.

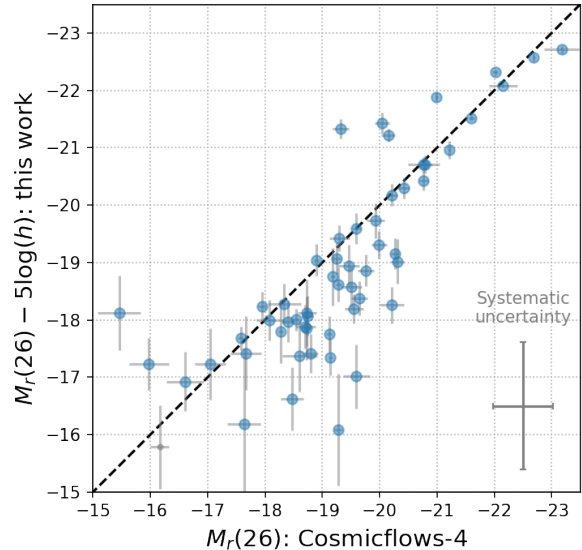


Figure 11. Comparison of the absolute magnitudes computed using our calibrated TFR and that of Cosmicflows-4 (Kourkchi et al. 2020a). Galaxies considered dwarfs by our calibration (M_r fainter than the line perpendicular to the calibrated TFR at $M_r = -17$) are shown in small gray points. The black dashed line corresponds to $y = x$. We find excellent agreement with their TFR.

the peculiar velocity for each of the 1136 galaxies using the Watkins & Feldman (2015) estimator. We show the log distance ratio (the ratio of the distance to the galaxy measured using redshift to that from the calibrated TFR) for our sample as a function of redshift in Fig. 10. The distances measured from our calibrated TFR and resulting peculiar velocities for the 1136 galaxies in our sample are given in Table 3.

In both Fig. 9 and 10, we see a significant scatter towards small rotational velocities and negative peculiar velocities. After visual inspection, we find that the majority of galaxies more than 2σ from the calibrated TFR are either interacting systems, irregular galaxies, or relatively face-on spiral galaxies whose photometric position angles are likely misaligned with their kinematic position angles. We look forward to eliminate some of this contamination with more accurate morphological classifications in future data releases, and we recommend using these galaxies' peculiar velocities with caution.

7. DISCUSSION

7.1. Comparison with CosmicFlows-4

For galaxies observed as part of the DESI PV Survey EDR that have velocity widths observed in the ALFALFA H I survey (Haynes et al. 2018), we can compare our TFR calibration with the Cosmicflows-4 TFR (Kourkchi et al. 2020a). Because we measure the veloc-

Table 3. DESI EDR Peculiar Velocities from the TFR

SGA-2020 ID	R.A. [deg]	Decl. [deg]	Redshift	$D(26)$ [arcmin]	$m_r(26)$ [AB mag]	$V(0.33R_{26})$ [km/s]	μ [AB mag]	V_{pec} [km/s]
896	180.381827	1.295827	0.02243(3)	0.62	15.92 ± 0.005	64 ± 15	33.32 ± 0.92	3100 ± 3000
1548	252.860800	33.034304	0.06211(2)	0.54	17.07 ± 0.010	145 ± 10	37.01 ± 0.39	-4700 ± 3300
1583	236.811826	43.995408	0.03547(2)	0.44	17.31 ± 0.016	64.8 ± 6.2	34.65 ± 0.46	2700 ± 2200
1980	221.076523	0.044044	0.02825(2)	1.05	14.66 ± 0.009	316 ± 12	37.75 ± 0.32	-11900 ± 1300
2497	240.338401	42.491513	0.04404(2)	0.50	15.61 ± 0.011	197.1 ± 5.6	36.90 ± 0.32	-7400 ± 1900

NOTE—Five of the 1136 galaxies in DESI EDR with peculiar velocities measured using the calibrated TFR. Sky positions and diameters of the 26 mag arcsec^{-2} isophote in the r -band are from the SGA-2020 (Moustakas et al. 2023). Redshifts are measured from the DESI EDR spectra, and rotational velocities at $0.33R_{26}$ are computed as described in Sec. 4. Distance moduli are calculated from the calibrated TFR, and peculiar velocities are based on the difference between the observed redshift and that inferred from the distance moduli following Watkins & Feldman (2015). Table 3 is published in its entirety online in a machine-readable format. A portion is shown here for guidance regarding its form and content.

ities at different radii and use a different value for V_0 in the calibration, it is easiest to compare our results by comparing the absolute magnitudes computed for the same galaxies using these two calibrated TFRs. We compute the absolute magnitudes in the r -band with the distance moduli calculated by Eqn. 11 of Kourkchi et al. (2020a) using the parameters given in their Table 2. We restrict our galaxies to the same domain within which both our calibrations are valid: spiral galaxies with $i > 45^\circ$, a S/N > 10 in the observed ALFALFA H I velocity width, and an adjusted H I velocity width > 64 km/s.

The comparison between our TFRs is shown in Fig. 11 for the 56 galaxies that exist in both samples. We find excellent agreement with the Cosmicflows-4 TFR calibration of Kourkchi et al. (2020a). The scatter in our calibrated TFR, $\sigma_{\text{Coma}} = 1.07 \pm 0.02$ AB mag, is about twice as large as that of the Coma Cluster in the Cosmicflows-4 calibration (Kourkchi et al. 2020a); with less than half of the number of galaxies used in the calibration and calibrating with velocities at $0.33R_{26}$, this larger scatter is expected. We expect our intrinsic scatter to decrease in future DESI data releases, as we increase the radius at which we measure the rotational velocity to $0.4R_{26}$ and experiment with scaling the rotational velocities based on the surface brightness.

7.2. The slope of the TFR

As shown in Sec. 5.3, we measure a slope of -7.96 ± 0.13 AB mag for the TFR. In the form of Eqn. 3, this corresponds to a power-law exponent of 3.18 ± 0.05 . This is smaller than the generally-accepted model expectation of 4, consistent with the results of Yegorova & Salucci (2007), who show that the slope of the TFR monotonically increases with the radius at which the velocity is measured. Along this same line, we should then expect our slope to be slightly smaller than TFR slopes calibrated with H I line widths, as the H I velocity probes the kinematics to full extent of the gaseous disk. Indeed, we find that our slope is smaller than the calibrated slopes of the TFR for the r -band by, e.g., Ponomareva et al. (2017) and Kourkchi et al. (2020a).

8. CONCLUSION

We present a calibration of the Tully-Fisher relation (TFR) using observations collected in the DESI Peculiar Velocity (PV) Survey during the DESI Survey’s Survey Validation (SV) period. This secondary targeting program places fibers on the centers and major axes of spatially-resolved spiral galaxies within the DESI sky footprint, allowing us to measure the rotational velocities of the galaxies at $0.33R_{26}$ for 1163 spiral galaxies.

We use an iterative process to calibrate the TFR, so as to perform the calibration without dwarf galaxies. We fit for the TFR using galaxies in the Coma Cluster, the only cluster observed during DESI SV with a high enough galaxy count to perform this calibration, and two galaxies observed in DESI SV with calibrated distances from SN Ia, with four free parameters: the slope, y -intercepts of the Coma Cluster and galaxies with known distances, and the intrinsic scatter in the Coma Cluster’s TFR. We then calculate the line perpendicular to the Coma Cluster’s TFR that intersects the cluster’s TFR at an apparent magnitude corresponding to $M_r = -17$ at the distance of the Coma Cluster, and we remove any galaxies within the Coma Cluster that are fainter than this line. We repeat this process (fitting for the slope and y -intercepts) until we converge on a fixed set of non-dwarf galaxies in Coma. This results in 41 galaxies in Coma used to fit for a slope of -7.96 ± 0.13 AB mag in the r -band for velocities at $0.33R_{26}$. The calibrated zero point is $-19.34^{+0.30}_{-0.29}$ AB mag.

This work serves as a proof-of-concept for the analysis using the full 5-year DESI PV Survey. The substantial increase in sample size will greatly reduce the uncertainties in our calibrated Tully-Fisher relation and will permit the measure of the peculiar motion of more than 53,000 disk galaxies (Saulder et al. 2023) in the local universe, composing the largest sample of disk galaxies with measured peculiar velocities to date.

ACKNOWLEDGEMENTS

The authors thank former NSF REU undergraduate students Grace Chiodo, for her help with the SDSS MaNGA comparisons, and Hayley Nofi, for her help implementing the subclassed version of Hyperfit. This material is based on work supported in part by the National Science Foundation Grant No. PHY-1757062 and PHY-2149332 and the Department of Energy Grant No. SC0008475. Data shown in figures, as well as example Python code to generate the figures, are available on Zenodo at <https://doi.org/10.5281/zenodo.15794231>.

This material is based upon work supported by the U.S. Department of Energy (DOE), Office of Science, Office of High-Energy Physics, under Contract No. DE-AC02-05CH11231, and by the National Energy Research Scientific Computing Center, a DOE Office of Science User Facility under the same contract. Additional support for DESI was provided by the U.S. National Science Foundation (NSF), Division of Astronomical Sciences under Contract No. AST-0950945 to the NSF’s National Optical-Infrared Astronomy Re-

search Laboratory; the Science and Technology Facilities Council of the United Kingdom; the Gordon and Betty Moore Foundation; the Heising-Simons Foundation; the French Alternative Energies and Atomic Energy Commission (CEA); the National Council of Humanities, Science and Technology of Mexico (CONAH-CYT); the Ministry of Science, Innovation and Universities of Spain (MICIU/AEI/10.13039/501100011033), and by the DESI Member Institutions: <https://www.desi.lbl.gov/collaborating-institutions>. Any opinions, findings, and conclusions or recommendations expressed in this material are those of the author(s) and do not necessarily reflect the views of the U.S. National Science

Foundation, the U.S. Department of Energy, or any of the listed funding agencies.

The authors are honored to be permitted to conduct scientific research on I'oligam Du'ag (Kitt Peak), a mountain with particular significance to the Tohono O'odham Nation.

Software: Astropy (Astropy Collaboration et al. 2013, 2018, 2022), Corner (Foreman-Mackey 2016), HyperFit (Robotham & Obreschkow 2015), Kcorrect (Blanton & Roweis 2007), Matplotlib (Hunter 2007), NumPy (Harris et al. 2020), SciPy (Virtanen et al. 2020)

REFERENCES

- Aaronson, M., Huchra, J., & Mould, J. 1979, *ApJ*, 229, 1, doi: [10.1086/156923](https://doi.org/10.1086/156923)
- Abazajian, K. N., Adelman-McCarthy, J. K., Agüeros, M. A., et al. 2009, *ApJS*, 182, 543, doi: [10.1088/0067-0049/182/2/543](https://doi.org/10.1088/0067-0049/182/2/543)
- Abdurro'uf, Accetta, K., Aerts, C., et al. 2022, *ApJS*, 259, 35, doi: [10.3847/1538-4365/ac4414](https://doi.org/10.3847/1538-4365/ac4414)
- Astropy Collaboration, Robitaille, T. P., Tollerud, E. J., et al. 2013, *A&A*, 558, A33, doi: [10.1051/0004-6361/201322068](https://doi.org/10.1051/0004-6361/201322068)
- Astropy Collaboration, Price-Whelan, A. M., Sipőcz, B. M., et al. 2018, *AJ*, 156, 123, doi: [10.3847/1538-3881/aabc4f](https://doi.org/10.3847/1538-3881/aabc4f)
- Astropy Collaboration, Price-Whelan, A. M., Lim, P. L., et al. 2022, *ApJ*, 935, 167, doi: [10.3847/1538-4357/ac7c74](https://doi.org/10.3847/1538-4357/ac7c74)
- Barrera-Ballesteros, J. K., Heckman, T., Sánchez, S. F., et al. 2018, *ApJ*, 852, 74, doi: [10.3847/1538-4357/aa9b31](https://doi.org/10.3847/1538-4357/aa9b31)
- Blanton, M. R., & Moustakas, J. 2009, *ARA&A*, 47, 159, doi: [10.1146/annurev-astro-082708-101734](https://doi.org/10.1146/annurev-astro-082708-101734)
- Blanton, M. R., & Roweis, S. 2007, *AJ*, 133, 734, doi: [10.1086/510127](https://doi.org/10.1086/510127)
- Boruah, S. S., Hudson, M. J., & Lavaux, G. 2020a, *MNRAS*, 498, 2703, doi: [10.1093/mnras/staa2485](https://doi.org/10.1093/mnras/staa2485)
- . 2020b, *MNRAS*, 498, 2703, doi: [10.1093/mnras/staa2485](https://doi.org/10.1093/mnras/staa2485)
- Bottinelli, L., Gougouenheim, L., Paturel, G., & de Vaucouleurs, G. 1983, *A&A*, 118, 4
- Bundy, K., Bershady, M. A., Law, D. R., et al. 2015, *ApJ*, 798, 7, doi: [10.1088/0004-637X/798/1/7](https://doi.org/10.1088/0004-637X/798/1/7)
- Burkey, D., & Taylor, A. N. 2004, *MNRAS*, 347, 255, doi: [10.1111/j.1365-2966.2004.07192.x](https://doi.org/10.1111/j.1365-2966.2004.07192.x)
- Burstein, D. 1982, *ApJ*, 253, 539, doi: [10.1086/159656](https://doi.org/10.1086/159656)
- Chaussidon, E., Yèche, C., Palanque-Delabrouille, N., et al. 2023, *ApJ*, 944, 107, doi: [10.3847/1538-4357/acb3c2](https://doi.org/10.3847/1538-4357/acb3c2)
- Colless, M., Saglia, R. P., Burstein, D., et al. 2001, *MNRAS*, 321, 277, doi: [10.1046/j.1365-8711.2001.04044.x](https://doi.org/10.1046/j.1365-8711.2001.04044.x)
- Cooper, A. P., Kogosov, S. E., Allende Prieto, C., et al. 2023, *ApJ*, 947, 37, doi: [10.3847/1538-4357/acb3c0](https://doi.org/10.3847/1538-4357/acb3c0)
- Davis, M., Nusser, A., Masters, K. L., et al. 2011, *MNRAS*, 413, 2906, doi: [10.1111/j.1365-2966.2011.18362.x](https://doi.org/10.1111/j.1365-2966.2011.18362.x)
- Davis, M., Nusser, A., & Willick, J. A. 1996, *ApJ*, 473, 22, doi: [10.1086/178124](https://doi.org/10.1086/178124)
- Davis, T. M., & Scrimgeour, M. I. 2014, *MNRAS*, 442, 1117, doi: [10.1093/mnras/stu920](https://doi.org/10.1093/mnras/stu920)
- DESI Collaboration, Aghamousa, A., Aguilar, J., et al. 2016a, arXiv e-prints, arXiv:1611.00037, doi: [10.48550/arXiv.1611.00037](https://doi.org/10.48550/arXiv.1611.00037)
- . 2016b, arXiv e-prints, arXiv:1611.00036. <https://arxiv.org/abs/1611.00036>
- DESI Collaboration, Abareshi, B., Aguilar, J., et al. 2022, *AJ*, 164, 207, doi: [10.3847/1538-3881/ac882b](https://doi.org/10.3847/1538-3881/ac882b)
- DESI Collaboration, Adame, A. G., Aguilar, J., et al. 2024a, *AJ*, 168, 58, doi: [10.3847/1538-3881/ad3217](https://doi.org/10.3847/1538-3881/ad3217)
- . 2024b, *AJ*, 167, 62, doi: [10.3847/1538-3881/ad0b08](https://doi.org/10.3847/1538-3881/ad0b08)
- . 2024c, arXiv e-prints, arXiv:2411.12022, doi: [10.48550/arXiv.2411.12022](https://doi.org/10.48550/arXiv.2411.12022)
- DESI Collaboration, Abdul-Karim, M., Adame, A. G., et al. 2025a, arXiv e-prints, arXiv:2503.14745, doi: [10.48550/arXiv.2503.14745](https://doi.org/10.48550/arXiv.2503.14745)
- DESI Collaboration, Abdul-Karim, M., Aguilar, J., et al. 2025b, arXiv e-prints, arXiv:2503.14738, doi: [10.48550/arXiv.2503.14738](https://doi.org/10.48550/arXiv.2503.14738)
- Dey, A., Schlegel, D. J., Lang, D., et al. 2019, *AJ*, 157, 168, doi: [10.3847/1538-3881/ab089d](https://doi.org/10.3847/1538-3881/ab089d)
- Djorgovski, S., & Davis, M. 1987, *ApJ*, 313, 59, doi: [10.1086/164948](https://doi.org/10.1086/164948)
- Dressler, A., Lynden-Bell, D., Burstein, D., et al. 1987, *ApJ*, 313, 42, doi: [10.1086/164947](https://doi.org/10.1086/164947)
- Drory, N., MacDonald, N., Bershady, M. A., et al. 2015, *AJ*, 149, 77, doi: [10.1088/0004-6256/149/2/77](https://doi.org/10.1088/0004-6256/149/2/77)

- Flaugher, B., Diehl, H. T., Honscheid, K., et al. 2015, *AJ*, 150, 150, doi: [10.1088/0004-6256/150/5/150](https://doi.org/10.1088/0004-6256/150/5/150)
- Foreman-Mackey, D. 2016, *The Journal of Open Source Software*, 1, 24, doi: [10.21105/joss.00024](https://doi.org/10.21105/joss.00024)
- Gorski, K. M., Davis, M., Strauss, M. A., White, S. D. M., & Yahil, A. 1989, *ApJ*, 344, 1, doi: [10.1086/167771](https://doi.org/10.1086/167771)
- Graziani, R., Courtois, H. M., Lavaux, G., et al. 2019, *MNRAS*, 488, 5438, doi: [10.1093/mnras/stz078](https://doi.org/10.1093/mnras/stz078)
- Groth, E. J., Juskiewicz, R., & Ostriker, J. P. 1989, *ApJ*, 346, 558, doi: [10.1086/168038](https://doi.org/10.1086/168038)
- Guy, J., Bailey, S., Kremin, A., et al. 2023, *AJ*, 165, 144, doi: [10.3847/1538-3881/acb212](https://doi.org/10.3847/1538-3881/acb212)
- Hahn, C., Wilson, M. J., Ruiz-Macias, O., et al. 2023, *AJ*, 165, 253, doi: [10.3847/1538-3881/acff8](https://doi.org/10.3847/1538-3881/acff8)
- Harris, C. R., Millman, K. J., van der Walt, S. J., et al. 2020, *Nature*, 585, 357, doi: [10.1038/s41586-020-2649-2](https://doi.org/10.1038/s41586-020-2649-2)
- Haynes, M. P., Giovanelli, R., Kent, B. R., et al. 2018, *ApJ*, 861, 49, doi: [10.3847/1538-4357/aac956](https://doi.org/10.3847/1538-4357/aac956)
- Hong, T., Staveley-Smith, L., Masters, K. L., et al. 2019, *MNRAS*, 487, 2061, doi: [10.1093/mnras/stz1413](https://doi.org/10.1093/mnras/stz1413)
- Howlett, C. 2019, *MNRAS*, 487, 5209, doi: [10.1093/mnras/stz1403](https://doi.org/10.1093/mnras/stz1403)
- Howlett, C., Robotham, A. S. G., Lagos, C. D. P., & Kim, A. G. 2017a, *ApJ*, 847, 128, doi: [10.3847/1538-4357/aa88c8](https://doi.org/10.3847/1538-4357/aa88c8)
- Howlett, C., Said, K., Lucey, J. R., et al. 2022, *MNRAS*, 515, 953, doi: [10.1093/mnras/stac1681](https://doi.org/10.1093/mnras/stac1681)
- Howlett, C., Staveley-Smith, L., & Blake, C. 2017b, *MNRAS*, 464, 2517, doi: [10.1093/mnras/stw2466](https://doi.org/10.1093/mnras/stw2466)
- Howlett, C., Staveley-Smith, L., Elahi, P. J., et al. 2017c, *MNRAS*, 471, 3135, doi: [10.1093/mnras/stx1521](https://doi.org/10.1093/mnras/stx1521)
- Hunter, J. D. 2007, *Computing in Science & Engineering*, 9, 90, doi: [10.1109/MCSE.2007.55](https://doi.org/10.1109/MCSE.2007.55)
- Johnson, A., Blake, C., Koda, J., et al. 2014, *MNRAS*, 444, 3926, doi: [10.1093/mnras/stu1615](https://doi.org/10.1093/mnras/stu1615)
- Jones, D. H., Saunders, W., Colless, M., et al. 2004, *MNRAS*, 355, 747, doi: [10.1111/j.1365-2966.2004.08353.x](https://doi.org/10.1111/j.1365-2966.2004.08353.x)
- Kaiser, N. 1988, *MNRAS*, 231, 149, doi: [10.1093/mnras/231.2.149](https://doi.org/10.1093/mnras/231.2.149)
- Koda, J., Blake, C., Davis, T., et al. 2014, *MNRAS*, 445, 4267, doi: [10.1093/mnras/stu1610](https://doi.org/10.1093/mnras/stu1610)
- Koribalski, B. S., Staveley-Smith, L., Westmeier, T., et al. 2020, *Ap&SS*, 365, 118, doi: [10.1007/s10509-020-03831-4](https://doi.org/10.1007/s10509-020-03831-4)
- Kourkchi, E., Tully, R. B., Anand, G. S., et al. 2020a, *ApJ*, 896, 3, doi: [10.3847/1538-4357/ab901c](https://doi.org/10.3847/1538-4357/ab901c)
- Kourkchi, E., Tully, R. B., Eftekharzadeh, S., et al. 2020b, *ApJ*, 902, 145, doi: [10.3847/1538-4357/abb66b](https://doi.org/10.3847/1538-4357/abb66b)
- Lai, Y., Howlett, C., & Davis, T. M. 2023, *MNRAS*, 518, 1840, doi: [10.1093/mnras/stac3252](https://doi.org/10.1093/mnras/stac3252)
- Lan, T.-W., Tojeiro, R., Armengaud, E., et al. 2023, *ApJ*, 943, 68, doi: [10.3847/1538-4357/aca5fa](https://doi.org/10.3847/1538-4357/aca5fa)
- Levi, M., Bebek, C., Beers, T., et al. 2013, arXiv e-prints, arXiv:1308.0847, doi: [10.48550/arXiv.1308.0847](https://doi.org/10.48550/arXiv.1308.0847)
- Miller, T. N., Doel, P., Gutierrez, G., et al. 2024, *AJ*, 168, 95, doi: [10.3847/1538-3881/ad45fe](https://doi.org/10.3847/1538-3881/ad45fe)
- Mould, J. 2020, *Frontiers in Astronomy and Space Sciences*, 7, 21, doi: [10.3389/fspas.2020.00021](https://doi.org/10.3389/fspas.2020.00021)
- Moustakas, J., Lang, D., Dey, A., et al. 2023, *ApJS*, 269, 3, doi: [10.3847/1538-4365/acfaa2](https://doi.org/10.3847/1538-4365/acfaa2)
- Myers, A. D., Moustakas, J., Bailey, S., et al. 2023, *AJ*, 165, 50, doi: [10.3847/1538-3881/aca5f9](https://doi.org/10.3847/1538-3881/aca5f9)
- Nusser, A., & Davis, M. 1994, *ApJ*, 421, L1, doi: [10.1086/187172](https://doi.org/10.1086/187172)
- Park, C. 2000, *MNRAS*, 319, 573, doi: [10.1046/j.1365-8711.2000.03886.x](https://doi.org/10.1046/j.1365-8711.2000.03886.x)
- Park, C.-G., & Park, C. 2006, *ApJ*, 637, 1, doi: [10.1086/498258](https://doi.org/10.1086/498258)
- Phillips, M. M. 1993, *ApJL*, 413, L105, doi: [10.1086/186970](https://doi.org/10.1086/186970)
- Pierce, M. J., & Tully, R. B. 1988, *ApJ*, 330, 579, doi: [10.1086/166495](https://doi.org/10.1086/166495)
- Ponomareva, A. A., Verheijen, M. A. W., Peletier, R. F., & Bosma, A. 2017, *MNRAS*, 469, 2387, doi: [10.1093/mnras/stx1018](https://doi.org/10.1093/mnras/stx1018)
- Poppett, C., Tyas, L., Aguilar, J., et al. 2024, *AJ*, 168, 245, doi: [10.3847/1538-3881/ad76a4](https://doi.org/10.3847/1538-3881/ad76a4)
- Qin, F., Howlett, C., & Staveley-Smith, L. 2019, *MNRAS*, 487, 5235, doi: [10.1093/mnras/stz1576](https://doi.org/10.1093/mnras/stz1576)
- Qin, F., Parkinson, D., Hong, S. E., & Sabiu, C. G. 2023, *JCAP*, 2023, 062, doi: [10.1088/1475-7516/2023/06/062](https://doi.org/10.1088/1475-7516/2023/06/062)
- Qin, F., Parkinson, D., Howlett, C., & Said, K. 2021, *ApJ*, 922, 59, doi: [10.3847/1538-4357/ac249d](https://doi.org/10.3847/1538-4357/ac249d)
- Raichoor, A., Moustakas, J., Newman, J. A., et al. 2023, *AJ*, 165, 126, doi: [10.3847/1538-3881/acb213](https://doi.org/10.3847/1538-3881/acb213)
- Ravi, N., Douglass, K. A., & Demina, R. 2024, *ApJ*, 967, 135, doi: [10.3847/1538-4357/ad36c2](https://doi.org/10.3847/1538-4357/ad36c2)
- Robotham, A. S. G., & Obreschkow, D. 2015, *PASA*, 32, e033, doi: [10.1017/pasa.2015.33](https://doi.org/10.1017/pasa.2015.33)
- Said, K., Colless, M., Magoulas, C., Lucey, J. R., & Hudson, M. J. 2020, *MNRAS*, 497, 1275, doi: [10.1093/mnras/staa2032](https://doi.org/10.1093/mnras/staa2032)
- Said, K., Howlett, C., Davis, T., et al. 2025, *MNRAS*, 539, 3627, doi: [10.1093/mnras/staf700](https://doi.org/10.1093/mnras/staf700)
- Sandage, A., & Tammann, G. A. 1976, *ApJ*, 210, 7, doi: [10.1086/154798](https://doi.org/10.1086/154798)
- Saulder, C., Howlett, C., Douglass, K. A., et al. 2023, *MNRAS*, 525, 1106, doi: [10.1093/mnras/stad2200](https://doi.org/10.1093/mnras/stad2200)
- Schlafly, E. F., Kirkby, D., Schlegel, D. J., et al. 2023, *AJ*, 166, 259, doi: [10.3847/1538-3881/ad0832](https://doi.org/10.3847/1538-3881/ad0832)

- Shi, Y., Zhang, P., Mao, S., & Gu, Q. 2024, *MNRAS*, 528, 4922, doi: [10.1093/mnras/stae274](https://doi.org/10.1093/mnras/stae274)
- Silber, J. H., Fagrelus, P., Fanning, K., et al. 2023, *AJ*, 165, 9, doi: [10.3847/1538-3881/ac9ab1](https://doi.org/10.3847/1538-3881/ac9ab1)
- Smee, S. A., Gunn, J. E., Uomoto, A., et al. 2013, *AJ*, 146, 32, doi: [10.1088/0004-6256/146/2/32](https://doi.org/10.1088/0004-6256/146/2/32)
- Sofue, Y., & Rubin, V. 2001, *ARA&A*, 39, 137, doi: [10.1146/annurev.astro.39.1.137](https://doi.org/10.1146/annurev.astro.39.1.137)
- Springob, C. M., Masters, K. L., Haynes, M. P., Giovanelli, R., & Marinoni, C. 2007, *ApJS*, 172, 599, doi: [10.1086/519527](https://doi.org/10.1086/519527)
- Stahl, B. E., de Jaeger, T., Boruah, S. S., et al. 2021, *MNRAS*, 505, 2349, doi: [10.1093/mnras/stab1446](https://doi.org/10.1093/mnras/stab1446)
- Taylor, E. N., Cluver, M., Bell, E., et al. 2023, *The Messenger*, 190, 46, doi: [10.18727/0722-6691/5312](https://doi.org/10.18727/0722-6691/5312)
- Tonry, J., & Schneider, D. P. 1988, *AJ*, 96, 807, doi: [10.1086/114847](https://doi.org/10.1086/114847)
- Tully, R. B. 2015, *AJ*, 149, 171, doi: [10.1088/0004-6256/149/5/171](https://doi.org/10.1088/0004-6256/149/5/171)
- Tully, R. B., & Fisher, J. R. 1977, *A&A*, 54, 661
- Tully, R. B., Howlett, C., & Pomarède, D. 2023a, *ApJ*, 954, 169, doi: [10.3847/1538-4357/aceaf3](https://doi.org/10.3847/1538-4357/aceaf3)
- Tully, R. B., & Pierce, M. J. 2000, *ApJ*, 533, 744, doi: [10.1086/308700](https://doi.org/10.1086/308700)
- Tully, R. B., Rizzi, L., Shaya, E. J., et al. 2009, *AJ*, 138, 323, doi: [10.1088/0004-6256/138/2/323](https://doi.org/10.1088/0004-6256/138/2/323)
- Tully, R. B., Kourkchi, E., Courtois, H. M., et al. 2023b, *ApJ*, 944, 94, doi: [10.3847/1538-4357/ac94d8](https://doi.org/10.3847/1538-4357/ac94d8)
- Turner, R. J., Blake, C., & Ruggeri, R. 2021, *MNRAS*, 502, 2087, doi: [10.1093/mnras/stab212](https://doi.org/10.1093/mnras/stab212)
- . 2023, *MNRAS*, 518, 2436, doi: [10.1093/mnras/stac3256](https://doi.org/10.1093/mnras/stac3256)
- Virtanen, P., Gommers, R., Oliphant, T. E., et al. 2020, *Nature Methods*, 17, 261, doi: [10.1038/s41592-019-0686-2](https://doi.org/10.1038/s41592-019-0686-2)
- Watkins, R., & Feldman, H. A. 2015, *MNRAS*, 450, 1868, doi: [10.1093/mnras/stv651](https://doi.org/10.1093/mnras/stv651)
- Whitford, A. M., Howlett, C., & Davis, T. M. 2022, *MNRAS*, 513, 345, doi: [10.1093/mnras/stac783](https://doi.org/10.1093/mnras/stac783)
- Yegorova, I. A., & Salucci, P. 2007, *MNRAS*, 377, 507, doi: [10.1111/j.1365-2966.2007.11637.x](https://doi.org/10.1111/j.1365-2966.2007.11637.x)
- York, D. G., Adelman, J., Anderson, John E., J., et al. 2000, *AJ*, 120, 1579, doi: [10.1086/301513](https://doi.org/10.1086/301513)
- Zhou, R., Dey, B., Newman, J. A., et al. 2023, *AJ*, 165, 58, doi: [10.3847/1538-3881/aca5fb](https://doi.org/10.3847/1538-3881/aca5fb)
- Zhou, R., Guy, J., Kopolov, S. E., et al. 2024, *arXiv e-prints*, arXiv:2409.05140, doi: [10.48550/arXiv.2409.05140](https://doi.org/10.48550/arXiv.2409.05140)
- Zou, H., Zhou, X., Fan, X., et al. 2017, *PASP*, 129, 064101, doi: [10.1088/1538-3873/aa65ba](https://doi.org/10.1088/1538-3873/aa65ba)